Ramos, C., Mechie, J., Stiller, M. (2018): Reflection seismic images and amplitude ratio modelling of the Chilean subduction zone at 38.25°S. - *Tectonophysics*, *747-748*, pp. 115—127.

DOI: http://doi.org/10.1016/j.tecto.2018.10.007

Reflection seismic images and amplitude ratio modelling of the Chilean subduction zone at 38.25°S.

C. Ramos[a,b*], J. Mechie[a], and M. Stiller[a]

[a]Deutsches GeoForschungsZentrum GFZ, Sections "Geophysical Deep Sounding" and "Near-surface Geophysics", Telegrafenberg, 14473 Potsdam, Germany

[b]University of Potsdam, Institute of Earth and Environmental Science

[*]E-mail: c.ramos.domke@gmail.com

Keywords: Reflection seismics – Reflectivity method – Subduction zone – South America.

Abstract

Active source near-vertical reflection (NVR) data from the interdisciplinary project TIPTEQ were used to image and identify structural and petrophysical properties within the Chilean subduction zone at 38.25°S, where in 1960 the largest earthquake ever recorded (M_w 9.5) occurred. Reflection seismic images of the subduction zone were obtained using the post-stack depth migration technique to process the three components of the NVR data, allowing to present P- and S-stacked time sections and depth-migrated seismic reflection images. Next, the reflectivity method allowed to model traveltimes and amplitude ratios of pairs of reflections for two 1D profiles along the studied transect. The 1D seismic velocities that produced the synthetic seismograms with amplitudes and traveltimes that fit the observed ones were used to infer the rock composition of the different layers in each 1D profile. Finally, an image of the subduction zone is given. The Chilean subduction zone at 38.25°S underlies a continental crust with highly reflective horizontal, as well as dipping events. Among them, the Lanalhue Fault Zone (LFZ), interpreted to be east-dipping, is imaged to very shallow depths for the first time. In terms of seismic velocities, the inferred composition

of the continental crust is in agreement with field geology observations at the surface along the profile. Furthermore, no measurable amounts of fluids above the plate interface in the continental crust in this part of the Chilean subduction zone are necessary to explain the results. A large-scale anisotropy in the continental crust and upper mantle is qualitatively proposed. However, quantitative studies on this topic in the continental crust of the Chilean subduction zone at 38.25°S do not exist to date.

1 Introduction

Many earthquakes of great magnitude occur in the seismically coupled part of subduction zones such as the active continental margin of southern Chile. Here, several earthquakes of magnitude greater than 8 have been recorded, including the greatest ever recorded to date with M_w 9.5 (Fig. 1), thus making this seismogenic zone one of high scientific interest.

Substantial knowledge about the structures, processes and properties within the seismogenic coupling zone of southern Chile has been obtained over the last years through geophysical programs such as ISSA-2000 (Integrated Seismological experiment in the Southern Andes; Lüth et al., 2003; Bohm, 2004), SPOC (Subduction Processes Off Chile; Krawczyk and the SPOC Team, 2003) and TIPTEQ (from The Incoming Plate to mega-Thrust EarthQuake processes). The TIPTEQ project, which comprised multi-disciplinary subprojects, aimed to investigate the thermal state and structure of the oceanic plate and the subduction zone, the seismicity and nucleation of large subduction-related earthquakes, the rheology and composition of the subducting sediments and the role of water in all of the above (Rietbrock et al., 2005; Scherwath et al., 2006).

In this work, active source near-vertical reflection (NVR) data from TIPTEQ were used to obtain P- and S-wave seismic reflection images of the continental crust and the plate interface beneath the Coastal Cordillera and the Central Valley along an east-west profile at 38.25°S. Additionally, the reflectivity method was used to model synthetic amplitude ratios of pairs of reflectivity bands, which allowed to infer the possible composition of the different layers in the continental crust using the synthetic input P- and S-velocities to search in a rocks and minerals catalogue. The aim of this paper is to obtain an integrative image of the continental crust and the plate interface in southern Chile, to quantitatively study their petrophysical properties, such as seismic velocities, Poisson's ratios and amount of fluids, and to characterize the rock types within the Chilean subduction zone.

2 Tectonics

Located at 38.25°S (see Fig. 1), the study area corresponds to the southern Chile margin, where the oceanic Nazca plate, with an age of ∼25 Ma (Sdrolias and Müller, 2006), subducts obliquely under the South American plate at an angle of N82.4°E and with a convergence rate of 6.65 cm a^{-1} (Kendrick et al., 2003). The western flank of the Andes in the study area consists of the Coastal Cordillera by the Pacific Ocean and the Central Valley just east of it. The latter is a basin formed by Oligocene-Miocene volcanic and sedimentary rocks, which are covered by Pliocene-Quaternary sediments (Melnick and Echtler, 2006). The Coastal Cordillera is composed mainly of metamorphic rocks. Here, distinction based on contrasting lithologies and tectono-metamorphic signatures is made between the western and the eastern series, which are separated by the NNW-SSE striking, sinistral Lanalhue fault zone (LFZ). Local seismic catalogues show ongoing seismic activity along this fault (Haberland et al., 2006). The western series, occurring southwest of 38.2°S, is a Late-Carboniferous to Triassic basal-accretionary forearc wedge complex (Glodny et al., 2008). The main lithologies are meta-turbidites, chlorite schists and minor metabasites, with local occurrences of cherts, serpentinites and sulphide bodies (Hervé, 1988; Glodny et al., 2008). The eastern series, a frontally-accreted complex located northeast of 38.2°S, consists of Permian-Carboniferous magmatic arc granitoids and associated metasediments (Hervé, 1988; Glodny et al., 2008). In the Late Carboniferous, around 300 Ma ago, the subduction process initiated in this region, with the LFZ as a normal fault separating the frontally accreted eastern series from the then exhuming western series. Later on, in the Early Permian, the segment of the LFZ between 37.8°S and 39.75°S transformed into a semi-ductile to brittle, sinistral strike–slip fault (Glodny et al., 2008).

3 TIPTEQ seismic data

The onshore active source experiment within TIPTEQ, which was carried out in January 2005, consisted of explosive sources executed every 1.5 km along a so-called common depth point (CDP) west-east trending profile at 38.25°S, starting approximately in Victoria in the east to Quidico at the Pacific Ocean (see Fig. 1). The CDP line was calculated with linear regression using GPS data along selected roads. Fig. 1 shows the geographic location of the shots along the receiver line.

For this work, the near-vertical incidence reflection (NVR) seismic data were used. The data consist of 76 shots, including three shots off the line in the east. The highest fold achieved was 8-fold. 955 receiver stations were used, each 100 m apart (projected on the CDP line). 180 stations, all with one 3-component geophone buried 20 - 40 cm deep, were deployed at once to form the active spread, giving a spread length of 18 km, which moved from east to west towards the ocean. The deployed receiver stations consisted of an Earth Data Logger (EDL) recording unit, which recorded in miniSEED continuous data format, with a sampling rate of 5 ms.

The experiment provided high resolution P-wave reflection seismic images at this part of the margin for the first time (Micksch, 2008; Groß et al., 2008). See e.g. Micksch (2008) for further information about the experiment setup, as well as for the initial raw data processing (e.g. data format conversion, creation of a parameter and field geometry database, surgical and top mutes).

4 Data processing

The NVR data processing prepared the seismic data for the post-stack depth migration of the vertical component to obtain P-reflection seismic images, and of both horizontal components to obtain S-reflection seismic images.

Unlike the vertical component processing flow that produced the P-wave reflection seismic images obtained by Micksch (2008) and Groß et al. (2008), the data processing shown here produced P-wave phase stack and migration images instead of envelope reflection seismic images. A similar workflow produced S-reflection seismic images by separately processing both horizontal NVR data components. As the CDP profile is E-W, the EW-component is the radial component and the NS-component is the transverse component. Table 1 shows the details of the processing sequences.

Differences between the seismic processing for S-reflectivity with respect to the processing of P-reflectivity include firstly the elevation statics. Unlike for P-wave seismic processing, time shifts from a constant velocity might not represent the best static correction for S-waves (e.g. for unconsolidated sediments such as those in the first kilometres depth, where S-velocities are close to zero).

Following Dohr (1985), the static corrections used for S-reflectivity processing used the topography and the S-wave velocities in the first kilometres depth along the TIPTEQ profile obtained by Ramos et al. (2016).

The selected bandpass filter for the S-wave processing (4 - 8 - 20 - 40 Hz) removed most of the groundroll. The remaining surface-wave data were removed using a surgical mute. 8 Hz was chosen instead of the 10 Hz of the bandpass filter in the P-reflectivity processing because inspection of the data showed that S-wave reflectivity signals are present at lower frequencies. The filter was also more restrictive with higher frequencies, since the observed S-wave reflectivity was in general of poorer quality than P-reflectivity and higher frequencies added unwanted noise. Additionally, a post-stack time and space variant bandpass filter was applied to the stacked S-reflectivity data. This filter removed low-frequency noise in the first seconds, contributing to a general improvement of the signal-to-noise ratio.

During the pre-stack processing, random noise was reduced by using a complex Wiener unit prediction filter before using the Tau-P transform for coherency enhancement. Otherwise, the transform also acted on the random noise and did not contribute to improving the contrast between real seismic reflections and noise. In the P-reflectivity processing sequence the unit prediction filter was not necessary.

The S-velocity model used for stacking and depth migration was an empirical model, as S-waves are more sensitive to velocity variations than P-waves. The use of this empirical velocity model introduced a slightly more constructive stack of traces when compared to velocity models obtained from other data sets.

4.1 Imaging results

The time stacked reflection seismic image in Fig. 2 shows coherent, horizontal and dipping reflections that are spatially continuous for tens of kilometres. In particular, three prominent east-dipping reflectivity bands are observed beneath the western portion of the profile, with the lowermost band at such depths that it corresponds to the plate interface. East of the LFZ, these three bands are joined by an uppermost fourth band. No reflector related to the continental Moho was found, but a west-dipping steep reflector at the eastern part of the profile, between 19 s and 27 s, also observed by Groß et al. (2008) and Micksch (2008) can be clearly observed. The stacked image has a higher noise level around 50 km at all times, thus making the identification of the different reflectivity bands here more difficult than in the rest of the profile. A quick test using a deconvolution operator before the bandpass filter resulted in an image of inferior overall quality (e.g. the plate interface was less evident). However, an event visible in the first 3 seconds near 50 km (see black arrow in Fig. 3) could be an indication of the geometry of the LFZ at shallower depths, which had not been imaged previously (Groß et al., 2008; Micksch, 2008) and was not identified without the deconvolution (see Fig. 2).

Fig. 4 shows for the S-waves the CDP phase-stacked time sections of the east-west and north-south components. Similar reflections as in the P-wave stack (Fig. 2) are observed. The appearance of the reflections is, however, more spread out over time and the signal-to-noise ratio is lower than for the P-stack. Nevertheless, for most of the S-wave reflections, an equivalent P-wave reflection can be found. The uppermost band joining the other three east of the LFZ (A in Fig. 4a) was not as constructively stacked in this case, but it can still be identified in the EW component. One explanation for its low amplitudes could be that the S-velocity contrast giving rise to this reflection band is not as high as the P-velocity contrast giving rise to the equivalent reflection band in the P-wave stack. Similar to the P-reflectivity stacks, no reflector related to the continental Moho was found. Additionally, no west-dipping steep reflector in the eastern part of the profile between $\sim$33 - 47 s (S-wave times) was observed in either of the two components. It could be that the signal-to-noise ratio did not allow the stacking process to be constructive enough to identify this reflection band above the noise.

In general, Fig. 4 shows that the quality of the stacking is higher on the EW component than on the NS component. The fact that the utilized velocities favour the stack on one component over the other might be an indication of crustal anisotropy. Evidence for possible crustal anisotropy was also observed in the Chilean subduction zone in tomographic studies (Ramos et al., 2016) and in studies of electrical resistivity (Brasse et al., 2009; Kapinos et al., 2016).

Although in general the reflectivity bands are better imaged in the EW component than in the NS component, the reflectors B, interpreted to be a Permo-Triassic accretionary wedge by Krawczyk et al. (2006), and C, the eastern end of the plate interface, are better imaged in the

NS component (see Fig. 4b). Additionally, reflector D was not observed either on the EW or the vertical component. Reflector E is better imaged in the horizontal components than in the vertical component and the east-dipping reflector F had not been previously imaged in the P-stacks. Although these reflectors in the easternmost part of the profile seem to be clearly stacked, their interpretation must be taken with caution, as they lie in a portion of the profile where the CDP fold is very low.

The post-stack depth migrated image for P-wave reflectivity (Fig. 5) has similar characteristics as the P-stack image, with several bent, dipping and horizontal reflectors. The strength of the reflections varies along the different reflectors (e.g. along the plate interface). Whereas the three prominent east-dipping reflectivity bands beneath the western portion maintain their separate character, the middle two of the four reflectivity bands below the eastern part seem to lose clarity as separate bands the further east one goes. The steep west-dipping reflector is migrated to a position that is almost perpendicular to the east-dipping plate interface, crossing it beyond the eastern end of the profile (which consisted of zero-padded traces). The image does not give information about this reflector at shallower depths. Micksch (2008) emphasizes that the recordable dip of a certain reflective feature at a certain position depends on the geometry and the length of the spread, a point to keep in mind when interpreting and discussing e.g. steep reflections at both ends of the profile. Typical migration artefacts can be seen at both ends of the image due to a coarser CDP fold. No coherent events are observed above $\sim$7 km depth.

Fig. 6 shows the post-stack depth migrated reflection seismic image using a deconvolution operator. Less noise in the first kilometres depth than in Fig. 5 seems to allow to follow the reflectivity event corresponding to the LFZ to shallower depths.

5 Amplitude ratios modelling

Velocity contrasts that would give rise to the observed reflectivity bands in two different portions of the TIPTEQ CDP profile (west- and east 1D profiles, WP and EP respectively, Figs. 1, 2 and 5) were modelled. This was done by matching the mean observed amplitude ratios of the P- and S-reflections in the two profiles to synthetic amplitude ratios derived from theoretical seismograms. These seismograms were calculated using the reflectivity method as described in Fuchs and Müller

(1971), with 1D P- and S-wave velocity models as input. Different studies, such as Fuchs and Müller (1971) and Choy et al. (1980) consider that the reflectivity method is appropriate to derive layered models of the Earth's crust. The reflectivity method has the weakness of being a 1D modelling method and thus it does not consider the dipping layer interfaces or reflectivity bands, such as those in the reflection seismic images of the TIPTEQ transect. With the purpose of comparing the effect of neglecting the dip of the reflectors by using a flat-layered model instead of a dipping model to calculate synthetic seismograms, a simple test was carried-out. Traveltimes and amplitudes of three different P- and S-reflections were calculated for seismograms obtained using a flat layer model and a dipping layer model. In the dipping model, a dip of 14° was used, which is similar to the dip derived for the prominent reflection bands in the TIPTEQ NVR data (e.g. Krawczyk et al., 2006 and references therein). A synthetic source was placed at 20 km along the profile. The amplitude ratios and traveltimes were calculated at 0 km offset. The comparison showed small traveltime differences and negligible amplitude ratio differences between the synthetic seismograms calculated using a flat layer model and a dipping layer model, with a dip of 14° (see Fig. S1).

5.1 Observed amplitude ratios

The western profile (WP) along the TIPTEQ CDP line is located at ∼23 km, and the eastern profile (EP) at ∼67 km. In both cases, clear reflectivity bands could be observed in the P- and S-reflection seismic images. Firstly, the P- and S-reflections to be modelled were identified and located in the time domain (see Figs. 2 and 4) and depth domain (see Fig. 5) for both profiles. Then, the vertical and radial components of the TIPTEQ NVR data were re-processed to obtain stacked images without amplitude enhancers such as the AGC because they change amplitudes in an artificial way. For each profile, 70 consecutive CDP locations around 23 and 67 km are chosen. For each CDP, the difference between the maximum and the minimum amplitude of the waveform in a time window containing the reflection of interest was exported and taken as the observed amplitude. Finally, for each pair of P- and S-reflections, the amplitude ratios along the 70 CDPs were obtained. The mean value and standard deviation were calculated for each amplitude ratio along the 70 CDPs. These mean amplitude ratios were the ones which were chosen to be modelled with the reflectivity method. The standard deviations defined the limits that were deemed to be acceptable for the variation in the modelled amplitude ratios with respect to the mean observed ratio.

In the western profile at 23 km, three reflections were chosen for modelling their amplitude ratios and arrival times: two intracrustal, here called $P_{i1}P$ and $P_{i2}P$, and their corresponding S-reflections $S_{i1}S$ and $S_{i2}S$ and one at the top of the oceanic crust, here called $P_{oc}P$, with the corresponding S-reflection $S_{oc}S$. In the eastern profile at 67 km, four reflections were chosen for modelling their amplitude ratios and arrival times: three intracrustal, $P_{i1}P$, $P_{i2}P$ and $P_{i3}P$, and their corresponding S-reflections $S_{i1}S$, $S_{i2}S$ and $S_{i3}S$ and one at the top of the oceanic crust, $P_{oc}P$ and the corresponding S-reflection $S_{oc}S$. Figs. 7 and 8 show the observed reflections and their arrival times in the stacked reflection seismic images, with amplitude enhancers for visualisation purposes. The observed P- and S-amplitude ratios along the 70 CDP, with the mean observed amplitude ratio and standard deviation are shown in Figs. S2 and S3.

5.2 Modelling results

To construct the 1D P- and S-wave velocity input models for the WP, the depths of the interfaces producing the reflections were observed in Fig. 5 and initial P-velocity values and contrasts were extracted from the SPOC South (at 38.25°S) velocity model (Krawczyk et al., 2006). For the input 1D S-velocity model, the values that were tested always maintained a Poisson's ratio greater than 0.2 and only varied reasonably with respect to the S-velocities of Ramos et al. (2016). Thus, a P-wave velocity contrast from 6.3 - 6.6 km s^{-1} at 13 km depth was used, providing the one necessary absolute velocity contrast needed for the amplitude modelling. For this profile, two 1D P- and S-wave velocity models were found among the tests that generated synthetic seismograms whose reflections fit the observed amplitude ratios and arrival times (see Fig. 9). Both velocity models are similar. In fact, the velocity contrasts at the interfaces are identical, except for the interface at 31 km depth (corresponding to the top of the oceanic crust), which produces the reflections $P_{oc}P$ and $S_{oc}S$. One of the models has a low velocity zone (LVZ) at this depth and thus the reflections $P_{oc}P$ and $S_{oc}S$ show inverse polarity with respect to the other reflections (see seismograms in Fig. 9). Note also at 13 km depth the high P-velocity and low S-velocity contrast, which could be an indication for a decrease downwards of the quartz content in the rocks.

The same considerations for the WP were made for the EP for arrival time windows, depths of interfaces, and input 1D velocity models. The second reflector, generating the phases $P_{i2}P$ and $S_{i2}S$ is considered to be the same event as the first reflector, generating the $P_{i1}P$ and $S_{i1}S$ phases, in the western portion. This is due to the eastward dip of the reflection bands. Thus, the same P-velocity contrast used previously for the $P_{i1}P$ reflection in the western portion was used initially for the $P_{i2}P$ reflection in the eastern profile, that is, from 6.3 - 6.6 km s^{-1} at 22 km depth ($\sim$8 s two-way time). Unlike the western portion, where P- and S-velocity models that fit the observations were found both with and without a LVZ, the absence of a LVZ in this profile could be discarded based on the tectonic geometry as, at 67 km in the TIPTEQ profile, the continental Moho and mantle, with a velocity of $\sim$7.2 km s^{-1} (Krawczyk et al., 2006) lie above the oceanic crust. Not to have a LVZ at the interface between the overlying continental mantle and the underlying oceanic crust would mean that the P-wave velocity of the oceanic crust should be greater than the value of $\sim$7.2 km s^{-1} for the continental mantle, which would be unrealistic.

For the EP profile, two P- and S-wave velocity models were found among the tests that produced synthetic seismograms that fit the observations (see Fig. 10). In this case, both models have a LVZ at 42 km depth. Once again, the velocity contrasts for each interface are the same in both models. The two models are shown as an illustration of the non-uniqueness of the possible 1D velocity models. The first model has a velocity gradient in the layer between the second and third reflections and the second model has a layer with a velocity gradient between the third and fourth reflections. Note the reverberations in the synthetic seismograms between the reflections produced at the top and at the bottom of the layers containing a velocity gradient. These are due to the approximation of the velocity gradient using steps and are nevertheless tiny compared to the signals of interest.

The input 1D P- and S-velocity models for both profiles shown here (Figs. 9 and 10), although non-unique, vary little with respect to those obtained in previous studies (e.g. Krawczyk et al. 2006; Micksch 2008; Haberland et al. 2009; Ramos et al. 2016). A comparison made for each profile and for each modelled amplitude ratio with respect to the mean observed ones showed that all of the modelled amplitude ratios lie within one standard deviation of the mean observed amplitude ratios (see Figs. S4 and S5). Although for both the WP and the EP, the two shown P- and S-velocity models that produce reflections that fit the observations differ, the absolute velocity contrasts are the same.

6 Discussion

To obtain a detailed image and knowledge of the petrophysical properties and rock types within the studied portion of the Chilean subduction zone at 38.25°S, the P- and S-wave post-stack reflection seismic images and the synthetic 1D P- and S-wave velocity models from synthetic seismograms and amplitude ratio modelling were correlated with the results of other studies in the subduction zone. Such studies included e.g. GPS data, magnetotellurics, field geology, thermomechanical and gravimetric research. The image can be observed in Fig. 11.

6.1 Hydration/dehydration processes in the subduction zone

High resistivity (∼100 - 1000 Ωm) is typical of dry, cold crust and upper mantle, while resistivity lower than ∼10 Ωm indicates the presence of a fluid phase such as partial melt and/or aqueous fluids (Unsworth and Rondenay, 2012). The presence of water generally reduces the seismic velocity of rocks and minerals, affecting especially the S-velocities. For example, Thorwart et al. (2015) find evidence of fluid release and melts in the mantle beneath the volcanic arc at 39°S in the form of reduced S-velocities, coinciding with low resistivity observations.

In the case of the Chilean subduction zone at 38.25°S, resistivity values indicating a dry, cold continental crust are observed, with local exceptions (Kapinos et al., 2016). One such exception lies near the coast, between 10 - 25 km depth (see Fig. 11). This high conductivity anomaly coincides with low P- and S-velocities (Haberland et al., 2009; Ramos et al., 2016), with high reflectivity as seen in the images in this work and also in Krawczyk et al. (2006), Micksch (2008) and Groß et al. (2008), and also with a portion of the margin where Völker and Stipp (2015) model fluids being released from the oceanic crust under the continental forearc. Although such fluids can e.g. accumulate along the plate boundary or migrate upwards along the decollement, the results indicate that they could migrate into the upper continental crust at least partially. A similar conductor has been observed in other subduction zones such as northern Cascadia and Costa Rica

(Kapinos et al., 2016). Another high conductivity anomaly in the crust obtained by Kapinos et al. (2016) is closely correlated to a zone of very low P- and S-velocities just beneath the surface, at ∼55 km along the TIPTEQ profile, reaching values as low as 2 and 1.7 km s^{-1}, respectively (Micksch, 2008; Ramos et al., 2016). This anomaly is located just east of the mapped LFZ (see Fig. 11). It is probably slightly offset from its true location and represents highly conductive and weathered sediments. The conductor related to the continental mantle wedge in the 2D resistivity model is in the 3D model less conductive and apparently not completely connected to the mantle wedge (Kapinos et al., 2016). Due to this difference between both models, this conductor is not further taken into account in the integrative interpretation.

Onshore, the resistivity model of Kapinos et al. (2016) and the P- and S-wave velocity models of the studied region (Haberland et al., 2009; Ramos et al., 2016) show no evidence for the presence of fluids released from e.g. the subducting sediments due to compaction dewatering and dehydration reactions. Offshore however, clear evidence for active fluid seepage at the seafloor in the rupture area of the M_w 8.8 Maule earthquake is shown by Geersen et al. (2016). This apparent difference between the onshore and offshore regimes is in agreement with the model of Völker and Stipp (2015), which showed fluids being released from the oceanic crust beneath the offshore part of the forearc but not beneath the onshore part covered by the profile presented in this study.

Different studies have found an effective, although qualitative, correlation between high reflectivity and zones of peak dehydration and/or elevated pore pressure (Ide et al. 2007; Saffer and Tobin 2011 and references therein). Hyndman and Peacock (2003) and Ide et al. (2007) have linked the updip limit of the seismogenic zone to evidence of anomalous porosity, low P-wave velocity and high reflectivity, suggesting elevated fluid pressure and extremely low effective stress. Their models for the downdip limit show high v_p/v_s ratios and reflectivity. Observations of low S-velocities and high Poisson's ratios in the subducted oceanic crust in Japan and southern Mexico have been linked to zones of high pore fluid pressure at 25 - 50 km depth and between the locations of the 350 - 450 °C isotherms (Saffer and Tobin, 2011). Although in theory, the width of the seismogenic zone should be controlled to first order by the plate temperatures, with 100 - 150 °C for the updip and 350 - 450 °C for the downdip limit (Völker et al., 2011), high seismicity is observed in different zones along the plate interface in the study area. One example is at depths greater than 40 km

(Bohm, 2004; Haberland et al., 2006), which was the preferred continental Moho depth of Micksch (2008), and where the continental Moho abutted against the oceanic crust (see Fig. 11). Völker et al. (2011) propose that the subduction channel extending even beneath the continental mantle could explain the seismicity in this zone. On the other hand, high microseismicity fading at ∼33 km depth is explained by Völker et al. (2011) as the subduction channel controlling the downdip seismic-aseismic transition, as the subducted and accreted (meta)sediments are much weaker than the surrounding rocks of the lower continental crust. Thus, the downdip limit of the seismogenic zone in southern Chile might be controlled by neither a particular crustal structure regime nor by the 450°C isotherm, which lies at ∼70 km depth, beneath the Central Valley in the thermal model of Völker et al. (2011), but by a combination of several factors. Additionally, Völker et al. (2011) propose that microseismicity might not represent the updip and downdip limits. In this work, the interpreted width of the seismogenic zone is in agreement with the one suggested by Haberland et al. (2009), extending from ∼20 - 50 km depth (see yellow line in Fig. 11). On the one hand, the updip seismic-aseismic transition coincides with high reflectivity, low P- and S-velocities and a zone of fluids being partially released from the oceanic crust. On the other hand, the interpreted downdip limit of the seismogenic zone coincides with the point where fluids are newly released from the oceanic crust and a high Poisson's ratio anomaly. In Maksymowicz et al. (2017) and Contreras-Reyes et al. (2017), the up-dip limit of the Maule earthquake is discussed, being significantly shallower than the 20 km depth proposed here for the up-dip limit of the seismogenic zone. An explanation could be that the rupture plane of a great earthquake extends further up-dip than what is usually defined as the up-dip limit of the seismogenic zone. The post-stack migration images show reflectivity increasing at ∼45 km depth (see Fig. 5). The S-reflectivity on the horizontal components at this depth is low in the EW component, but high in the NS component. This suggests that probably the stacking velocities in this part of the profile favor the NS over the EW component, indicating once again the possibility of a high-scale crustal anisotropy.

6.2 Updated structural image of the southern Chile subduction zone

In general, all the reflections are depth-migrated to about the same depths in every P- and S-reflection seismic image in this profile (S-wave depth-migrated images are not shown, as they should in theory look similar to their P-reflectivity equivalent, and although this is true in practice, the quality of the images is poorer). Differences are no larger than some kilometres, and they coincide with previous reflection seismic images as well (Krawczyk and the SPOC Team, 2003; Micksch, 2008; Groß et al., 2008). In the case of the S-reflection seismic images, it validates the empirical stacking velocities used during the seismic processing. The oceanic crust is imaged with different intensity along the profile, with especially high intensity in the eastern part, below ~45 km depth (see Fig. 5), attributed to a zone of high pore pressure and dehydration processes. An interpretation of the top of the oceanic crust was made using the events from the ISSA-2000 and TIPTEQ local seismicity catalogues along with the existing reflection seismic images (Ramos et al., 2016). The interpreted geometry of the top of the slab and the oceanic Moho results in an oceanic crust with ~7 - 8 km thickness, in agreement with previous reflectivity studies in the area (e.g. Rauch, 2005; Krawczyk et al., 2006; Micksch, 2008; Contreras-Reyes et al., 2008). The depth of the oceanic Moho in Fig. 11, which cannot be identified in the reflection seismic images using the TIPTEQ NVR data, was taken from the SPOC wide-angle velocity model (Krawczyk et al., 2006) and corresponds to the depth where the P-velocity attains 8 km s^{-1}.

The depth of the continental Moho used in this work for the integrative interpretation is the same as that in Micksch (2008), at ~40 km depth, which is also the depth at which the P-wave velocities from the SPOC wide-angle model reach 7.2 km s^{-1}. The continental Moho is not observed in the TIPTEQ NVR data, probably due to the dewatering of the oceanic crust, which results in serpentinized forearc mantle material that reduces the velocity contrast between the continental crust and the mantle (Groß et al., 2008; Micksch, 2008). No method shows with complete certainty the continental Moho. The depth of the Moho from the gravity modelling of Alasonati-Tašárová (2007) depends on how the high density body in the continental wedge is interpreted. This high-density body overlaps a zone of reduced velocities and there is not a unique interpretation that explains the preferred modelled densities, as well as low P-velocities and high Poisson's ratios. It has been discussed whether this body represents exclusively ~20 - 30% hydrated mantle or if it is mafic crustal material, or a combination of both (Krawczyk et al., 2006). The Moho from the SPOC model is simply defined as the depth at which the P-velocities reach 7.2 km s^{-1}. It is located at 40 km depth, just east of the hypocentre of the M_w 9.5 Valdivia earthquake, as located by Krawczyk and the SPOC Team (2003). Although this interpretation alone of the continental Moho is not conclusive, it agrees with the interpreted continental Moho at 39°S from receiver functions of Yuan et al. (2006).

Haberland et al. (2009) observe low P-velocities of ~7 km s^{-1} which would imply a 35% serpentinized mantle wedge, but low v_p/v_s values at the base of the forearc which do not support a large scale serpentinization of the mantle wedge. They interpret this zone as lower crust at depths greater than 35 km, formed by dragged crustal material and they also observed small ~20% serpentinization clusters. In particular, a high Poisson's ratio anomaly is related to low P- and S-velocities and high conductivity, as well as high dehydration (Haberland et al., 2009; Völker and Stipp, 2015; Kapinos et al., 2016; Ramos et al., 2016). On the other hand, the Poisson's ratios next to it can reach values as low as ~0.23 (or v_p/v_s ratios of 1.69). Hacker and Abers (2012) suggest that unusually low v_p/v_s ratios of 1.65 (or Poisson's ratios of 0.21), with S-velocities of ~4.7 km s^{-1} can be an indicator of strongly anisotropic peridotites rather than unusual composition, due to a biased overestimation of S-velocities and/or underestimation of P-velocities, when compared to isotropic averages. Although the low Poisson's ratios in the continental mantle wedge are not as low, they are still lower than those for a typical subduction zone mantle wedge of 1.76 - 1.82 (Hacker and Abers, 2012). Similarly, the S-velocities are not as high as 4.7 km s^{-1} (Ramos et al., 2016). Thus, the interpretation for the continental mantle wedge in this region would be that velocities and Poisson's ratios are too low to be explained by purely serpentinized peridotite, although signs of serpentinization from different results are present in clusters. If anisotropy exists in the mantle wedge, it is not as strong as reported by Hacker and Abers (2012).

In the work of Becerra et al. (2013), at the latitude of the Arauco peninsula, they interpret a prominent fault system near the coast as the transition between the western series and the eastern series, but at 38.25°S this is not possible. Here, the presence of faults at the coast could represent a paleo-backstop as well, but more likely between what is offshore (presumably sediments) and the western series.

Some features not observed before this work include the steep east-dipping reflector observed in the EW S-reflection seismic image, located between ~85 - 95 km and 10 - 20 km depth. This reflector has a geometry which is probably difficult to be resolved due to the low data fold at the eastern end of the profile. Its nature will probably remain uncertain unless a new seismic experiment retrieves additional data further east. Another such feature is the reflector that has been interpreted as the east-dipping Lanalhue Fault Zone (LFZ, see Fig. 11). Although this reflector had been observed in the past, it was imaged up to ∼2 km depth in the P-wave post-stack migration image for the first time, using a deconvolution operator.

The true nature of the steep westward-dipping reflector that is prominent in the time and depth sections between 95 - 140 profile km beneath 30 km depth will remain uncertain unless more seismic data are collected. Due to the geometry of the seismic experiment, only the steep reflectivity has been recovered in the location of this reflector, as it lies beyond the eastern end of the profile. Furthermore, another possible artefact is that the imaged reflector will look larger than the actual reflector. A rheological boundary with ascending fluid paths, as found by Bloch et al. (2014) (and references therein) in northern Chile seems unlikely in this case. Firstly, no global or local seismic catalogue contains seismicity associated with the reflector, as it is located mainly in the aseismic continental mantle. Secondly, no related strong temperature gradient is proposed in this region (Völker et al., 2011). Thirdly, it is difficult to find high velocity contrasts or v_p/v_s anomalies in this region, because it lies at the limits of validity of the existent local models. The speculation of Groß et al. (2008), that this reflector is related to a possible ascent path for fluids and/or melts towards the volcanic arc is still the most reasonable hypothesis. However further research is required and should prove to give an interesting insight into the possible nature of this reflector.

6.3 Lithological units within the continental crust inferred from the reflectivity method

The synthetic 1D P- and S-velocities that produced synthetic seismograms with traveltimes and amplitude ratios of reflections that fit the observed ones were used to infer the composition and the rocks of different lithological units in the continental crust. This was done by matching the synthetic velocities to those in the catalogues of rocks and minerals from Stadtlander et al. (1999) and references therein, and Hacker and Abers (2004). The inferred units can be observed in Fig. 11.

Unit 1 is characterized by a general low Poisson's ratio anomaly with local elevated Poisson's ratios near the surface corresponding to unconsolidated sediments (Ramos et al., 2016). The lower limit of this layer at 5 km depth coincides with an intra-crustal discontinuity in the density model of Tassara and Echaurren (2012). It also coincides with seismic P- and S-velocity isolines of 6 and 3.4 km s^{-1}, respectively (Haberland et al., 2009; Ramos et al., 2016).

In the western profile, at 23 km, three amplitude ratios (or, equivalently, layer boundaries) were modelled. In the eastern profile, at 67 km, four reflections were modelled, but in this case only four layers were analysed, as the fifth layer, corresponding to the oceanic crust, lies deeper than 40 km. The laboratory samples used to produce the rocks and minerals catalogues were not exposed to such high pressures, so no information is available for this layer. The layers in the western profile are interpreted to extend to the eastern profile, so that for every reflection in the western profile, there is a reflection that originates at the same layer boundary in the eastern profile (see Fig. 11).

Unit 2 is interpreted to be the intrusive, granitic coastal batholith (covered by sediments near the surface). The modelled P- and S-velocities for this layer were 5.94 and 3.38 km s^{-1} respectively, with the consequent Poisson's ratio (σ) of 0.26. Example rock types found in the catalogues, which fit the velocities and σ in this layer, are granite, diorite and gneiss.

Unit 3 reaches depths of about 23 km in the eastern part. This layer had low S-reflectivity at the reflectors related to the LFZ and the Permo-Triassic accretionary wedge and thus the modelled velocity contrasts corresponding to those reflectors were very small (0.04 - 0.08 km s^{-1}). In the western part, the modelled P- and S-velocities for this layer were 6.1 - 6.3 and 3.4 - 3.72 km s^{-1} respectively, with $\sigma = 0.27$, whilst in the eastern part, they were about 6.3 and 3.46 km s^{-1}, with $\sigma = 0.28$. This layer was interpreted to be rich in amphibolite in the western part and changing to metabasite as it dips to greater depths towards the east. Additionally, rocks such as gneiss and gabbro are found to match the modelled velocities. Gabbro in particular, is observed exclusively in the western series (Hervé, 1988; Ardiles, 2003; Glodny et al., 2008) and its presence in this layer would again support an east-dipping LFZ.

Unit 4 has in the western part modelled P- and S-velocities of 6.6 and 3.76 km s^{-1} respectively, with σ of about 0.26. In the eastern part, slight variations of the modelled velocities that still fit the observations did not introduce great changes in the interpretation of the rocks in this layer. Such P- and S-velocities ranged in the eastern part between $\sim$6.6 - 7 and 3.7 - 3.85 km s^{-1} respectively, with σ $\sim$0.26 - 0.27. This layer was also interpreted to be amphibolite-rich in the western part, changing into granulite as it dips towards the east. Once again, gneiss and gabbro could also be present in this layer.

Unit 5 is constrained below by the oceanic crust. The modelled P- and S-velocities in the western part are 6.72 and 3.85 km s^{-1}, with σ slightly smaller than 0.26. As this layer dips in the eastern direction, it is interpreted to represent in part the continental mantle wedge. Modelled P- and S-velocities in this part of the profile are $\sim$6.9 - 7.3 and 4 - 4.2 km s^{-1}, resulting in σ ranging between values as low as 0.24 and 0.26. It is interesting that at 67 km a low Poisson's ratio anomaly reaching values as low as 0.23 can be identified in the continental mantle wedge. The interpretation of this layer in the western part is that it is more mafic than the overlying layers, with amphibolite starting to become granulite at these depths and with the presence of gabbro and serpentinized peridotite. As one moves to the east, gabbro could also be present in the eastern profile, but although the P- and S-velocities can be explained by 30% serpentinized peridotite (Hacker and Abers, 2004), which would be expected to be observed at these depths in a serpentinized mantle, the corresponding σ are not as low as the modelled ones. As suggested by Hacker and Abers (2012), anisotropy in peridotite in the continental mantle can explain that P- and/or S-velocities are biased with respect to their isotropic laboratory equivalents. Thus, the eastern part of this layer is interpreted to consist of two sub-layers, separated by the continental Moho (which is not identifiable in the observed reflectivity data): mafic, gabbro-rich lower crust, down to 40 km depth and above the continental mantle, which extends down to $\sim$45 km above the oceanic crust (reflectivity is observed starting at 42 km depth), with $\sim$20% anisotropic serpentinized peridotite, in agreement with Krawczyk et al. (2006) and Haberland et al. (2009).

Finally, the oceanic crust in the western profile has modelled P- and S-velocities near the top of the layer of $\sim$6.9 and 3.9 km s^{-1}, with σ of about 0.27. The rock found in the catalogue to match these observations is gabbro, which is in agreement with Haberland et al. (2009), who additionally suggest metamorphosed mid-oceanic ridge basalt (MORB) as a possible explanation for the observations.

The interpreted composition and rocks of each layer are in agreement with geological observations at the surface along the western and eastern series (Hervé, 1988; Ardiles, 2003; Burón, 2003; SERNAGEOMIN, 2003; Glodny et al., 2005; Melnick and Echtler, 2006; Glodny et al., 2008). The presence of rocks observed in the western series at 67 km along the TIPTEQ profile supports once again an east-dipping LFZ.

7 Conclusions

An updated structural image of the southern Chilean subduction zone at 38.25°S was obtained thanks to post-stack depth-migration P- and S-reflection seismic images and amplitude ratio modelling of seismic reflections. The S-reflection seismic images obtained in this work allowed to extend the knowledge of the structure and composition of the continental crust, as well as the possible geometry of the layers composing it. They also allowed to study the possible presence of fluids in terms of seismic velocities and reflected waves, which was one of the aims within the TIPTEQ project. The use of a deconvolution operator in the post-stack migrated P-reflectivity, although only quickly tested, helped to obtain information about the east-dipping Lanalhue Fault Zone (LFZ) closer to the surface for the first time.

The synthetic 1D P- and S-velocity models used to model seismic reflections whose traveltimes and amplitude ratios fit the observed ones, allowed a first order interpretation of the composition and rocks forming the different geological units in the continental crust. Although such input velocity models are non-unique, they do not vary greatly and the velocity contrasts between adjacent layers are more or less constant. The modelled velocities and Poisson's ratios show a continental crust consisting of east-dipping layers with compositions which are in agreement with geological observations along the profile. They show that Unit 2 (see units in Fig. 11) has a granitic composition, and is probably formed by rocks such as granite, diorite and gneiss. It is thus interpreted as the subsurface, intrusive coastal batholith. Unit 3 is interpreted to represent the Permo-Triassic accretionary wedge. This layer is interpreted to be amphibolite-rich in the western part, transitioning as it dips down into metabasite in the eastern part, with gneiss and gabbro as other possible rocks to be found. An elevated Poisson's ratio body in this layer (see Fig. 11) might represent granulite, gabbro or serpentinized peridotite (Ramos et al., 2016). Unit 4 is also interpreted as being amphibolite-rich in the west, changing to granulite as it dips towards the eastern part, with the possible presence of gneiss and gabbro. Unit 5, just above the oceanic crust, probably consists of gabbro, granulite and serpentinized peridotite in the western part. The eastern part of this layer, just east of the location of the M_w9.5 Valdivia earthquake, is interpreted to be divided into two sub-layers. The upper sub-layer, down to ~40 km depth, probably represents mafic, gabbro-rich lower continental crust. The sub-layer below, overlying the oceanic crust is interpreted as the continental mantle wedge, with clusters that could indicate a ~20% serpentinization of peridotite, but with Poisson's ratios lower than expected, based on isotropic velocities derived from laboratory samples.

Based on the interpretation of the composition of Units 3, 4 and 5 above the oceanic crust, rocks of the western series are interpreted to be present also in the eastern part of the profile either directly (e.g. gabbro) or as (higher-grade) metamorphic equivalents (e.g. metabasite, granulite). If the LFZ was purely vertical, no rocks of the western series should be present in the eastern part of the profile, as field geology studies do not report their presence at the surface. Thus, an east-dipping LFZ is inferred from seismic velocities, in agreement with geological and reflectivity observations.

From the conductors modelled from magnetotelluric data in the continental crust, only one near the coast should possibly be related to fluids in the continental crust. This high conductivity anomaly, although related to high P- and S-reflectivity, sporadically low P- and S- velocities and high pore pressure and dehydration, is not related to high Poisson's ratios. If fluids are present in this anomaly, they are not well detected by seismic velocities. In fact, the results from the seismic data suggest no measurable amounts of fluids above the plate interface in the continental crust in this part of the Chilean subduction zone.

The anisotropy topic was addressed several times in this work. The presence of a large-scale crustal – and upper-mantle – anisotropy would explain some observations, such as: stacking S-velocities resulting in certain reflectors that are better imaged in one horizontal component than in the other; inferred anisotropy in peridotite in the continental mantle wedge, observed as low Poisson's ratios not matching their isotropic laboratory equivalents. The presence of a large-scale crustal anisotropy has also been suggested by magnetotelluric studies in the region. Crustal anisotropy in the southern Chilean subduction zone is to date, however, not quantitatively studied. Such a research could possibly confirm or discard the hypotheses mentioned above.

The reflectivity in the eastern part of the profile and beyond should not be considered as conclusive due to the low data coverage in that part of the profile. For example, due to the field geometry, east-dipping reflectors in this zone are not recovered. The nature of the reflectors in this portion of the profile will probably remain uncertain until the TIPTEQ transect is extended further east.

Acknowledgements

The project TIPTEQ was funded by the German Ministry of Education and Research (BMBF), the German Research Foundation (DFG) and benefited from grants of the Free University of Berlin and the GFZ Potsdam. The instruments for the TIPTEQ experiments were provided by the Geophysical Instrument Pool Potsdam (GIPP) and the Free University of Berlin. The figures were made with the GMT program (Wessel et al., 2013). C. Ramos was supported by the German Academic Exchange Service (DAAD). The authors thank the editor Rob Govers and three anonymous reviewers whose comments helped to improve the manuscript.

References

Alasonati-Tašárová, Z., 2007: Towards understanding the lithospheric structure of the southern Chilean subduction zone (36°S–42°S) and its role in the gravity field, *Geophys. J. Int.*, **170**(3), 995–1014, URL `http://dx.doi.org/10.1111/j.1365-246X.2007.03466.x`.

Ardiles, M., 2003: La Serie Occidental del basamento metamórfico, centro sur de la Cordillera de Nahuelbuta, Chile, área Quidico-Capitán Pastene. Petrografía, mesoestructura y análisis microtectónico, Memoria de título, Dept. de Ciencias de la Tierra. Universidad de Concepción, Chile.

Becerra, J., Contreras-Reyes, E., and Arriagada, C., 2013: Seismic structure and tectonics of the southern Arauco Basin, south-central Chile (∼38°S), *Tectonophysics*, **592**(1), 53–66, URL `http://dx.doi.org/10.1016/j.tecto.2013.02.012`.

Bloch, W., Kummerow, J., Salazar, P., Wigger, P., and Shapiro, S.A., 2014: High-resolution image of the North Chilean subduction zone: seismicity, reflectivity and fluids, *Geophys. J. Int.*, **197**(3), 1744–1749, URL http://dx.doi.org/10.1093/gji/ggu084.

Bohm, M., 2004: 3D Lokalbebentomographie der südlichen Anden zwischen 36° und 40°S, Scientific technical report str04/15, Freie Universität Berlin and Deutsches GeoForschungsZentrum Potsdam, URL http://www.gfz-potsdam.de/bib/pub/str0415/0415.pdf.

Brasse, H., Kapinos, G., Li, Y., Mütschard, L., Soyer, W., and Eydam, D., 2009: Structural electrical anisotropy in the crust at the South-Central Chilean continental margin as inferred from geomagnetic transfer functions, *Phys. Earth Planet. Inter.*, **173**(1), 7–16, URL http://dx.doi.org/10.1016/j.pepi.2008.10.01.

Burón, P., 2003: Petrografía, estructuras y microtectónica del área de contacto entre las series metamórficas del basamento Paleozoico entre los 38°08' y 38°21'S, Cordillera de Nahuelbuta, Chile., Memoria de título, Dept. de Ciencias de la Tierra. Universidad de Concepción, Chile.

Choy, G., Cormier, V.F., Kind, R., Müller, G., and Richards, P.G., 1980: A comparison of synthetic seismograms of core phases generated by the full wave theory and by the reflectivity method, *Geophys. J Int.*, **61**(1), 21–39, URL http://dx.doi.org/10.1111/j.1365-246X.1980.tb04301.x.

Contreras-Reyes, E., Grevemeyer, I., Flüh, E.R., and Reichert, C., 2008: Upper lithospheric structure of the subduction zone offshore of southern Arauco peninsula, Chile, at ~38°S, *J. geophys. Res.*, **113**(B7), B07 303, URL http://dx.doi.org/10.1029/2007JB005569.

Contreras-Reyes, E., Maksymowicz, A., Lange, D., Grevemeyer, I., Muñoz Linford, P., and Moscoso, E., 2017: On the relationship between structure, morphology and large coseismic slip: A case study of the M_w 8.8 Maule, Chile 2010 earthquake., *Earth Planet. Sc. Lett.*, **478**, 27–39, URL http://dx.doi.org/10.1016/j.epsl.2017.08.028.

Dohr, G., 1985: Seismic Shear Waves: Theory, vol. 15A, Geophysical Press.

Fuchs, K. and Müller, G., 1971: Computation of synthetic seismograms with the reflectivity method and comparison with observations, *Geophys. J Int.*, **23**(4), 417–433, URL http://dx.doi.org/10.1111/j.1365-246X.1971.tb01834.x.

Geersen, J., Scholz, F., Linke, P., Schmidt, M., Lange, D., Behrmann, J.H., Völker, D., and Hensen, C., 2016: Fault zone controlled seafloor methane seepage in the rupture area of the 2010 Maule earthquake, Central Chile, *Geochem. Geophys. Geosyst.*, **17**(11), 4802–4813, URL http://dx.doi.org/10.1002/2016GC006498.

Glodny, J., Lohrmann, J., Echtler, H., Gräfe, K., Seifert, W., Collao, S., and Figueroa, O., 2005: Internal dynamics of a paleoaccretionary wedge: insights from combined isotope tectonochronology and sandbox modelling of the South-Central Chilean forearc, *Earth Planet. Sc. Lett.*, **231**(1), 23–39, URL http://dx.doi.org/10.1016/j.epsl.2004.12.014.

Glodny, J., Echtler, H., Collao, S., Ardiles, M., Burón, P., and Figueroa, O., 2008: Differential Late Paleozoic active margin evolution in South-Central Chile (37°S–40°S) – the Lanalhue Fault Zone, *J. South Am. Earth Sci.*, **26**(4), 397–411, URL http://dx.doi.org/10.1016/j.jsames.2008.06.001.

Groß, K., Micksch, U., and TIPTEQ research group, 2008: The reflection seismic survey of project TIPTEQ – the inventory of the Chilean subduction zone at 38°S, *Geophys. J Int.*, **172**(2), 565–571, URL http://dx.doi.org/10.1111/j.1365-246X.2007.03680.x.

Haberland, C., Rietbrock, A., Lange, D., Bataille, K., and Hoffmann, S., 2006: Interaction between forearc and oceanic plate at the southcentral Chilean margin as seen in local seismic data, *Geophys. Res. Lett.*, **33**(23), L23 302, URL http://dx.doi.org/10.1029/2006GL028189.

Haberland, C., Rietbrock, A., Lange, D., Bataille, K., and Dahm, T., 2009: Structure of the seismogenic zone of the south–central Chilean margin revealed by local earthquake travel–time tomography, *J. geophys. Res.*, **114**(B1), B01 317, URL http://dx.doi.org/10.1029/2008JB005802.

Hacker, B. and Abers, G., 2004: Subduction Factory 3: An Excel worksheet and macro for calculating the densities, seismic wave speeds, and H_2O contents of minerals and rocks at pressure and temperature, *Geochem. Geophys. Geosyst.*, **5**(1), URL http://dx.doi.org/10.1029/2003GC00061.

Hacker, B. and Abers, G., 2012: Subduction Factory 5: Unusually low Poisson's ratios in subduction zones from elastic anisotropy of peridotite, *J. geophys. Res.*, **117**(B6), B06 308, URL http://dx.doi.org/10.1029/2012JB009187.

Hervé, F., 1988: Late Paleozoic subduction and accretion in Southern Chile, *Episodes*, **11**(3), 183–188.

Hyndman, R. and Peacock, S., 2003: Serpentinization of the forearc mantle, *Earth planet. Sci. Lett.*, **212**(3–4), 417–432, URL http://dx.doi.org/10.1016/S0012-821X(03)00263-2.

Ide, S., Beroza, G.C., Shelly, D.R., and Uchide, T., 2007: A scaling law for slow earthquakes, *Nature*, **447**(7140), 76–79, URL http://dx.doi.org/10.1038/nature057.

Kapinos, G., Montahaei, M., Meqbel, N., and Brasse, H., 2016: Three-dimensional electrical resistivity image of the South-Central Chilean subduction zone, *Tectonophysics*, **666**(1), 76–89, URL http://dx.doi.org/10.1016/j.tecto.2015.10.016.

Kendrick, E., Bevis, M., Smalley, R., Brooks, B., Barriga Vargas, R., Lauría, E., and Soto Fortes, L.P., 2003: The Nazca–South America Euler vector and its rate of change, *J. South Am. Earth Sci.*, **16**(2), 125–131, URL http://dx.doi.org/10.1016/S0895-9811(03)00028-2.

Krawczyk, C. and the SPOC Team, 2003: Amphibious seismic survey images plate interface at 1960 Chile earthquake, *EOS, Trans. Am. geophys. Un.*, **84**(32), 301–305, URL http://dx.doi.org/10.1029/2003EO320001.

Krawczyk, C., Mechie, J., Lüth, S., Tašárová, Z., Wigger, P., Stiller, M., Brasse, H., Echtler, H., Araneda, M., and Bataille, K., 2006: Geophysical signatures and active tectonics at the south-central Chilean margin, in: The Andes – Active Subduction Orogeny. Frontiers in Earth Science, edited by Oncken, O., Chong, G., Franz, G., Giese, P., Götze, H., Ramos, V., Strecker, M., and Wigger, P., vol. 1, chap. 8, pp. 171–192, Springer Verlag, Berlin.

Lüth, S., Wigger, P., and ISSA Research Group, 2003: A crustal model along 39°S from a seismic refraction profile – ISSA 2000, *Revista Geológica de Chile*, **30**(1), 83–101, URL http://dx.doi.org/10.4067/S0716-02082003000100006.

Maksymowicz, A., Chadwell, C.D., Ruiz, J., Tréhu, A.M., Contreras-Reyes, E., Weinrebe, W., Díaz-Naveas, W.J., Gibson, J.C., Lonsdale, P., and Tryon, M.D., 2017: Coseismic seafloor de-formation in the trench region during the M_w8.8 Maule megathrust earthquake, *Sci. Rep.*, **7**, 45 918, URL http://dx.doi.org/10.1038/srep45918.

Melnick, D. and Echtler, H., 2006: Morphotectonic and geologic digital map compilations of the south-central Andes (36–43°S), in: The Andes – Active Subduction Orogeny. Frontiers in Earth Science, edited by Oncken, O., Chong, G., Franz, G., Giese, P., Götze, H., Ramos, V., Strecker, M., and Wigger, P., vol. 1, chap. 30, pp. 565–568, Springer Verlag.

Micksch, U., 2008: The Chilean subduction zone at 38.2°S: New geophysical images derived from seismic reflection data of project TIPTEQ; implications for the subduction channel and the seismogenic coupling zone, Scientific technical report str08/14, Freie Universität Berlin and Deutsches GeoForschungsZentrum Potsdam, URL http://www.gfz-potsdam.de/bib/pub/str0814/0814.pdf.

Ramos, C., Mechie, J., and Feng, M., 2016: Shear wave velocity and Poisson's ratio models across the southern Chile convergent margin at 38°15'S., *Geophys. J. Int.*, **204**(3), 1620–1635, URL http://dx.doi.org/10.1093/gji/ggv541.

Rauch, K., 2005: Cyclicity of Peru-Chile trench sediments between 36° and 38°S: a footprint of paleoclimatic variations?, *Geophys. Res. Lett.*, **32**(8), URL http://dx.doi.org/10.1029/2004GL022196.

Rietbrock, A., Haberland, C., Bataille, K., Dahm, T., and Oncken, O., 2005: Studying the seismogenic coupling zone with a passive seismic array, *EOS, Trans. Am. geophys. Un.*, **86**(32), 293–297, URL http://dx.doi.org/10.1029/2005EO320001.

Saffer, D. and Tobin, H., 2011: Hydrogeology and mechanics of subduction zone forearcs: Fluid flow and pore pressure, *Annu. Rev. Earth Planet. Sci.*, **39**, 157–186, URL http://dx.doi.org/10.1146/annurev-earth-040610-133408.

Scherwath, M., Flüh, E.R., Grevemeyer, I., Tilmann, F., Contreras-Reyes, E., and Weinrebe, W., 2006: Investigating subduction zone processes in Chile, *EOS, Trans. Am. geophys. Un.*, **87**(27), 265–272, URL http://dx.doi.org/10.1029/2006EO270001.

Sdrolias, M. and Müller, R. D., 2006: Controls on back-arc basin formation, *Geochem. Geophys. Geosyst.*, **7**(4), Q04 016, URL http://dx.doi.org/10.1029/2005GC001090.

SERNAGEOMIN, 2003: Mapa geológico de Chile, versión digital No. 4, Servicio Nacional de Geología y Minería, Santiago de Chile.

Stadtlander, R., Mechie, J., and Schulze, A., 1999: Deep structure of the southern Ural mountains as derived from wide-angle seismic data, *Geophys. J. Int.*, **137**(2), 501–515, URL http://dx.doi.org/10.1046/j.1365-246X.1999.00794.x.

Tassara, A. and Echaurren, A., 2012: Anatomy of the Andean subduction zone: three-dimensional density model upgraded and compared against global-scale models, *Geophys. J. Int.*, **189**(1), 161–168, URL http://dx.doi.org/10.1111/j.1365-246X.2012.05397.x.

Thorwart, M., Dzierma, Y., Lieser, K., Buhs, H., and Rabbel, W., 2015: Shear-wave velocity structure of the Chilean subduction zone (39-40°S) based on Rayleigh wave dispersion: evidence of fluid release and melts in the mantle beneath the Villarrica volcano, *Geological Society, London, Special Publications*, **410**(1), 59–70, URL http://dx.doi.org//10.1144/SP410.9.

Unsworth, M. and Rondenay, S., 2012: Mapping the distribution of fluids in the crust and lithospheric mantle utilizing geophysical methods, in: Metasomatism and the Chemical Transformation of Rock, chap. 13, pp. 535–598, Springer Berlin Heidelberg, URL dx.doi.org/10.1007/978-3-642-28394-9_13.

Völker, D. and Stipp, M., 2015: Water input and water release from the subducting Nazca Plate along southern Central Chile (33°S–46°S), *Geochem. Geophys. Geosyst.*, **16**(6), 1825–1847, URL http://dx.doi.org/10.1002/2015GC005766.

Völker, D., Grevemeyer, I., Stipp, M., Wang, K., and He, J., 2011: Thermal control of the seismogenic zone of southern central Chile, *J. geophys. Res.*, **116**(B10), B10 305, URL http://dx.doi.org/10.1029/2011JB008247.

Wessel, P., Smith, W. H.F., Scharroo, R., Luis, J., and Wobbe, F., 2013: Generic Mapping Tools: Improved version released, *EOS, Trans. Am. geophys. Un.*, **94**(45), 409–410, URL http://dx.doi.org/10.1002/2013EO450001.

Yuan, X., Asch, G., Bataille, K., Bock, G., Bohm, M., Echtler, H., Kind, R., Oncken, O., and Wölbern, I., 2006: Deep seismic images of the Southern Andes, in: Evolution of an Andean Margin: A tectonic and magmatic view from the Andes to the Neuquén Basin (35° - 39°S lat), vol. **407**, pp. 61–72, Geological Society of America, URL https://doi.org/10.1130/2006.2407(03).

Figures with captions

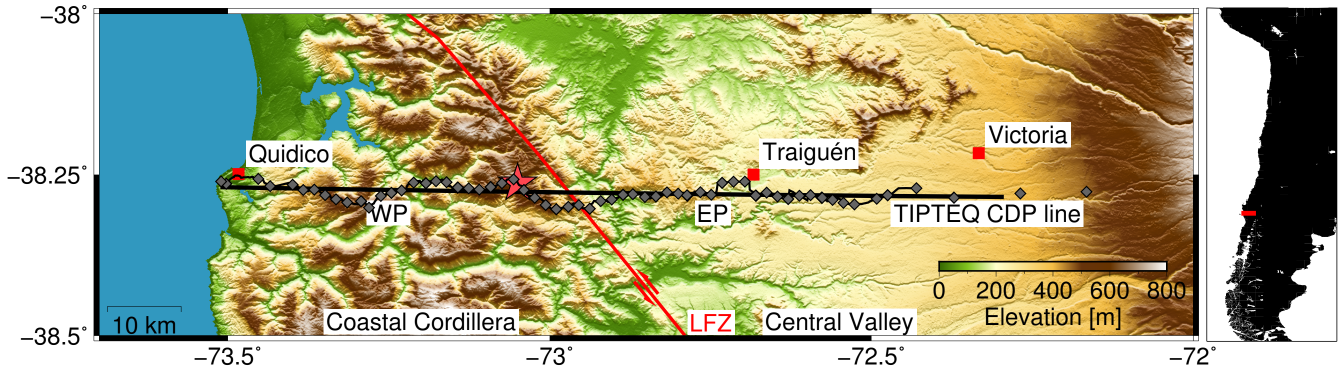

Figure 1: Location of TIPTEQ onshore active-source seismic experiment. Gray line: receiver line. Gray diamonds: shot locations. Black line: common depth-point (CDP) line of the TIPTEQ seismic reflection profile. Red star: epicentre of the 1960 Chilean earthquake after Krawczyk and the SPOC Team (2003). Red line: surface trace of the Lanalhue fault zone (LFZ; after Melnick and Echtler, 2006). WP/EP: West and east 1D profiles for which amplitude ratios were calculated using the reflectivity method.

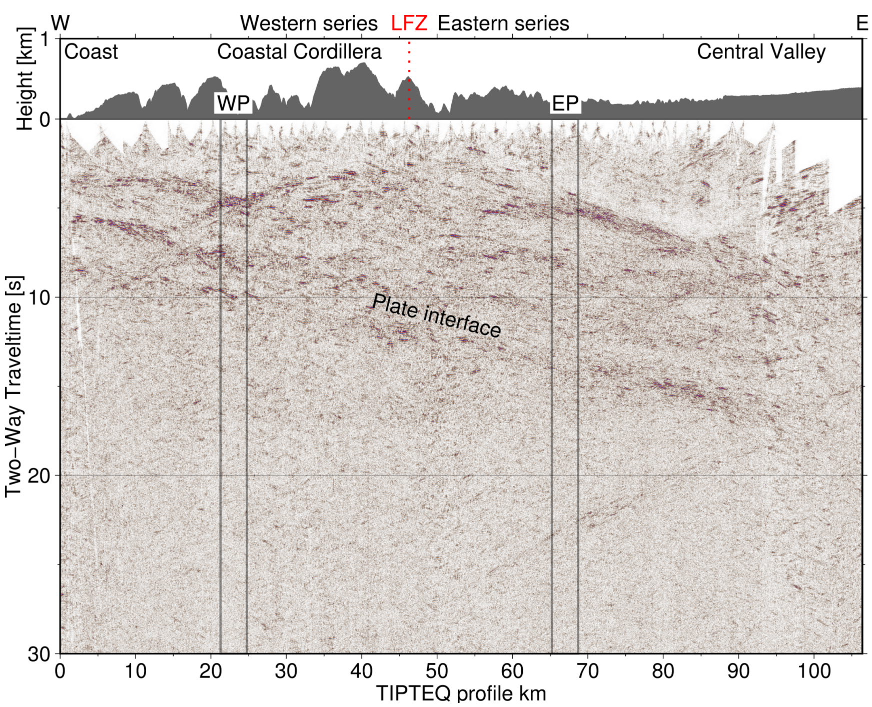

Figure 2: P-wave phase stack seismic reflection image derived from the vertical component of the seismic data along the TIPTEQ profile. WP and EP mark the rectangular regions for which synthetic seismograms were calculated and compared with the observed data. LFZ: Lanalhue Fault Zone.

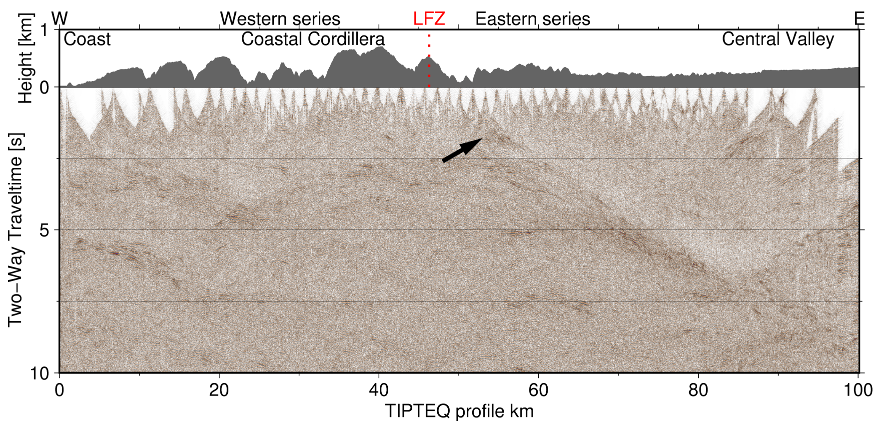

Figure 3: First 10 s of the P-wave phase stack with deconvolution. The black arrow points to what is interpreted as the geometry of the LFZ in the first seconds. LFZ: Lanalhue Fault Zone.

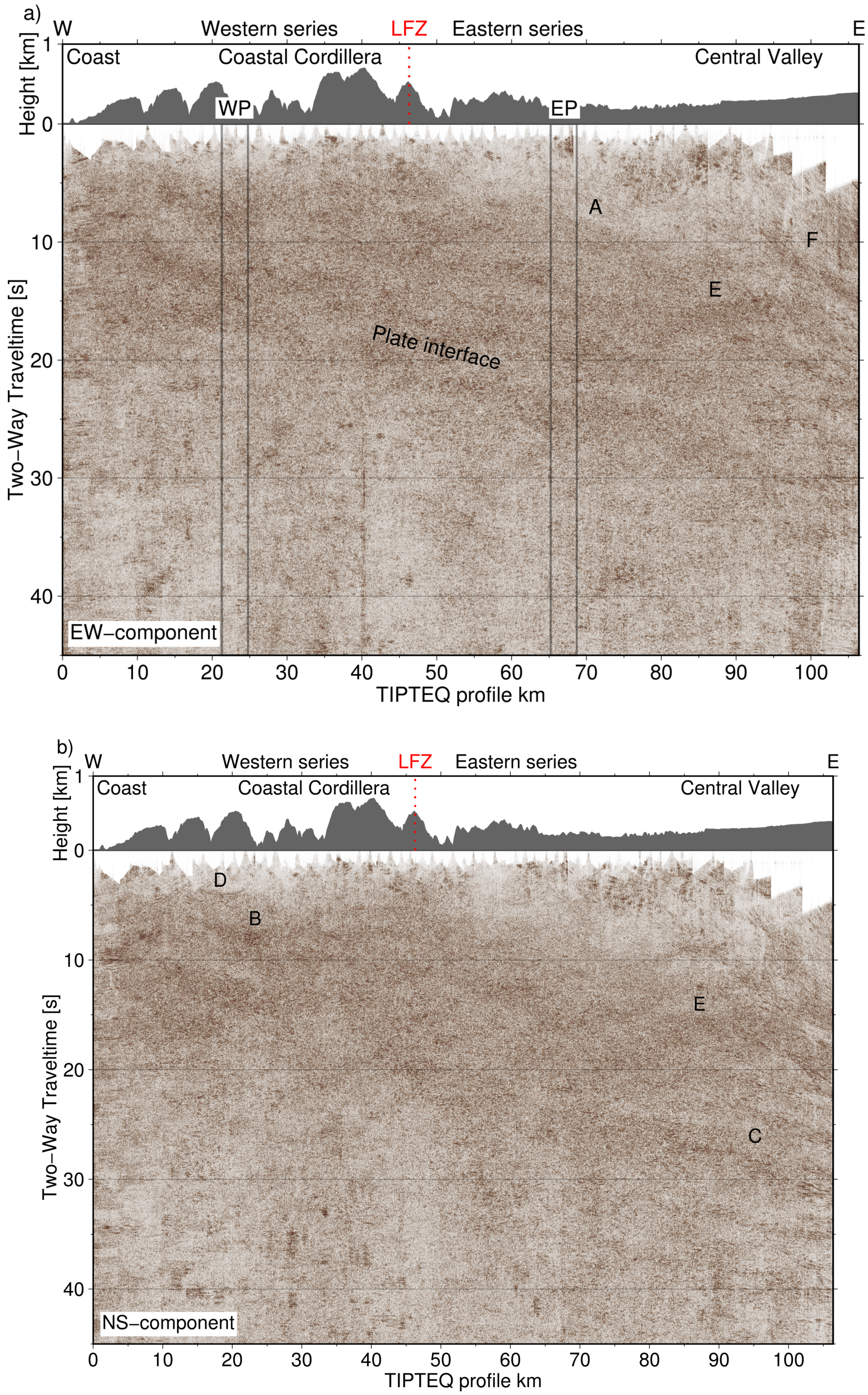

Figure 4: S-wave phase stack seismic reflection images of the horizontal components of the seismic data along the TIPTEQ profile. a) east-west component, b) north-south component. In a) the rectangles mark the regions for which synthetic seismograms were calculated. Letters marking features in the images are discussed in the text. LFZ: Lanalhue Fault Zone.

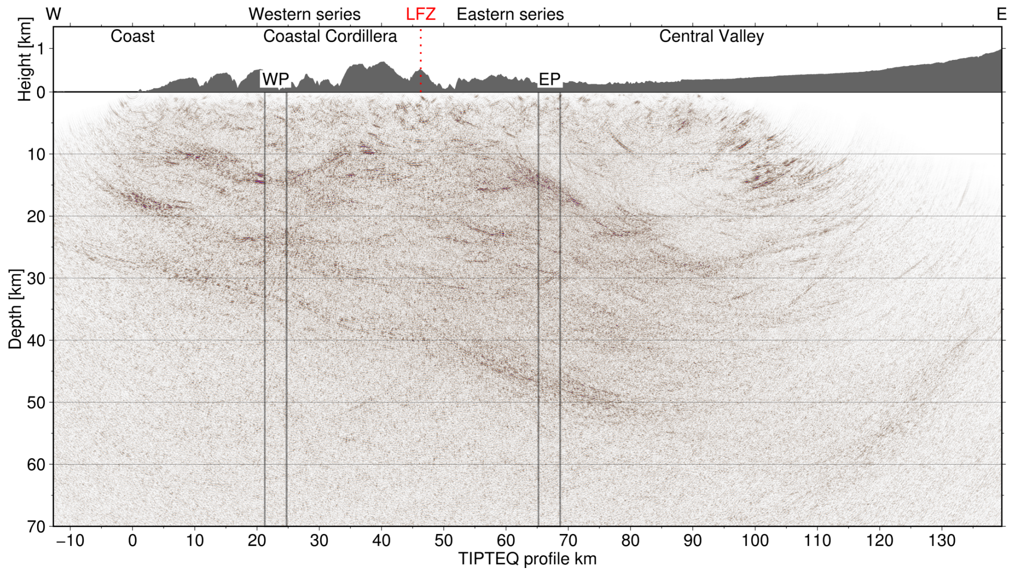

Figure 5: Post-stack depth migrated P-wave seismic reflection image. Vertical exaggeration ∼ 1. Synthetic seismograms using the reflectivity method were calculated for the two portions WP and EP inside the rectangles. LFZ: Lanalhue Fault Zone.

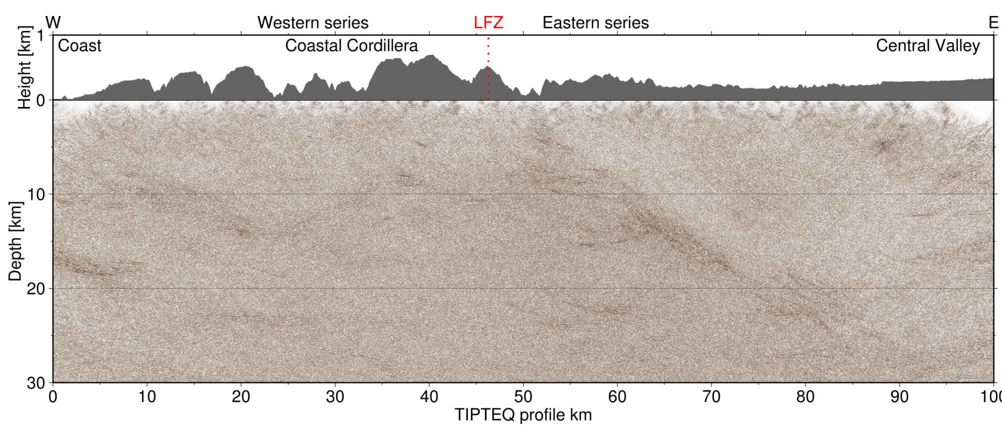

Figure 6: Close-up of post-stack depth migrated P-wave seismic reflection image with deconvolution. There are reflectivity candidates for the LFZ at shallower depths. Vertical exaggeration ∼ 1. LFZ: Lanalhue Fault Zone.

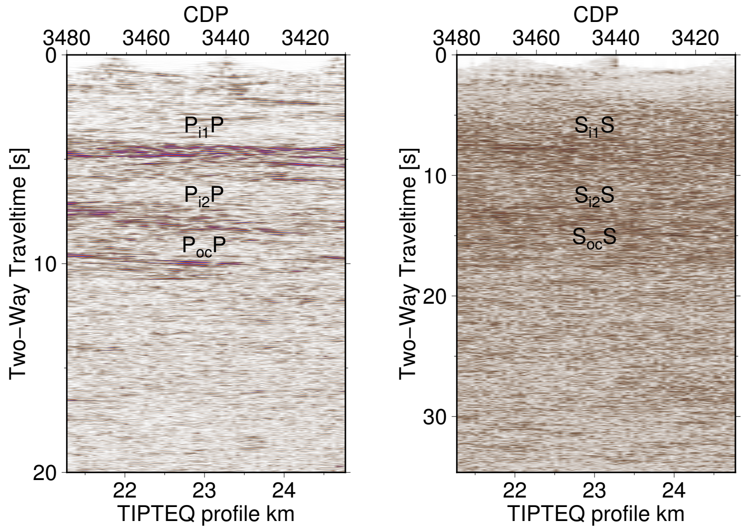

Figure 7: For the western 1D profile (WP), the three P- and S-reflections, whose arrival times and amplitude ratios were modelled using the reflectivity method. See also Fig. S2.

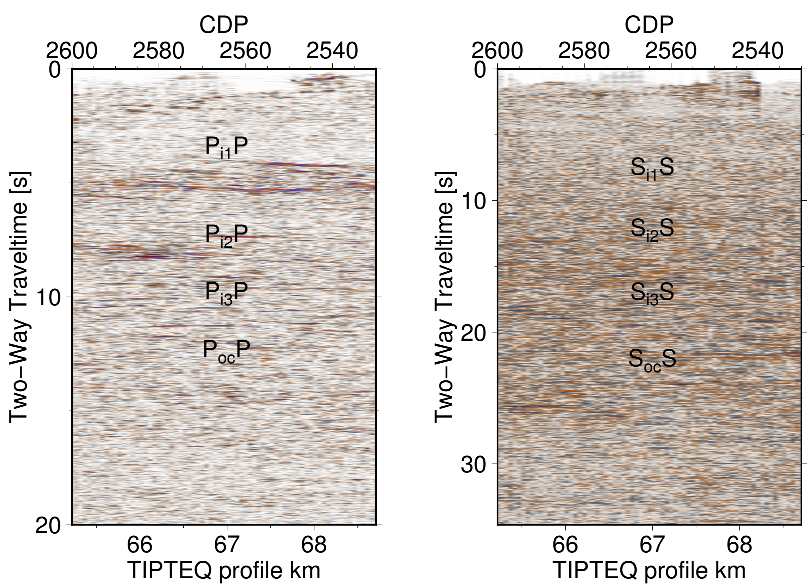

Figure 8: For the eastern 1D profile (EP), the four P- and S-reflections, whose arrival times and amplitude ratios were modelled using the reflectivity method. See also Fig. S3.

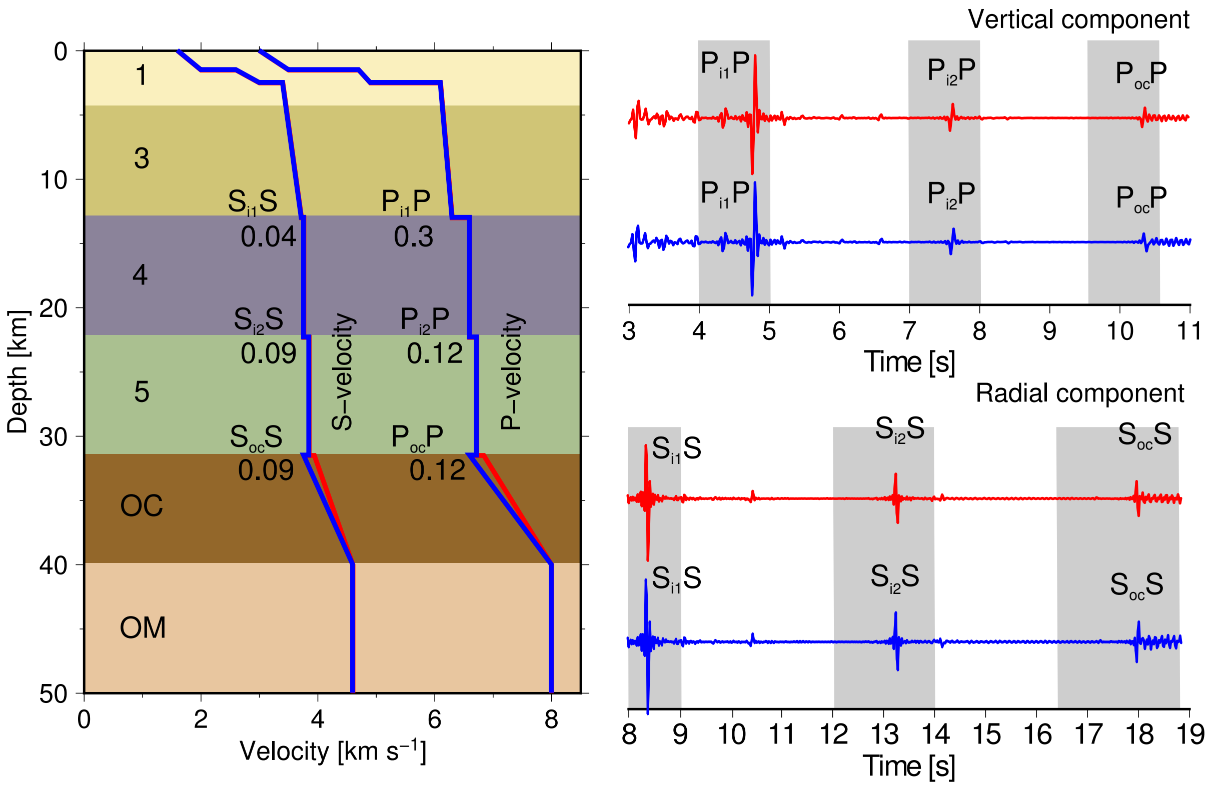

Figure 9: Left: synthetic 1D P- and S-velocity models found to reproduce the observed mean amplitude ratios in the western profile (WP). The numbers indicate the absolute values of the velocity contrasts at each interface in km s^{-1}. In blue: seismic velocity models with a low velocity zone (LVZ) at 31 km depth. In red: seismic velocity models without a LVZ. The colours and numbers of the layers indicate the inferred lithological units (see Section 6.3 and Fig. 11). OC: oceanic crust; OM: oceanic mantle. Right: synthetic seismograms with the modelled reflectivity phases. In blue: seismograms obtained from seismic velocity models with a LVZ. In red: seismograms obtained from seismic velocity models without a LVZ. The grey shading shows the time windows where the reflection phases were observed in the time-stacked images.

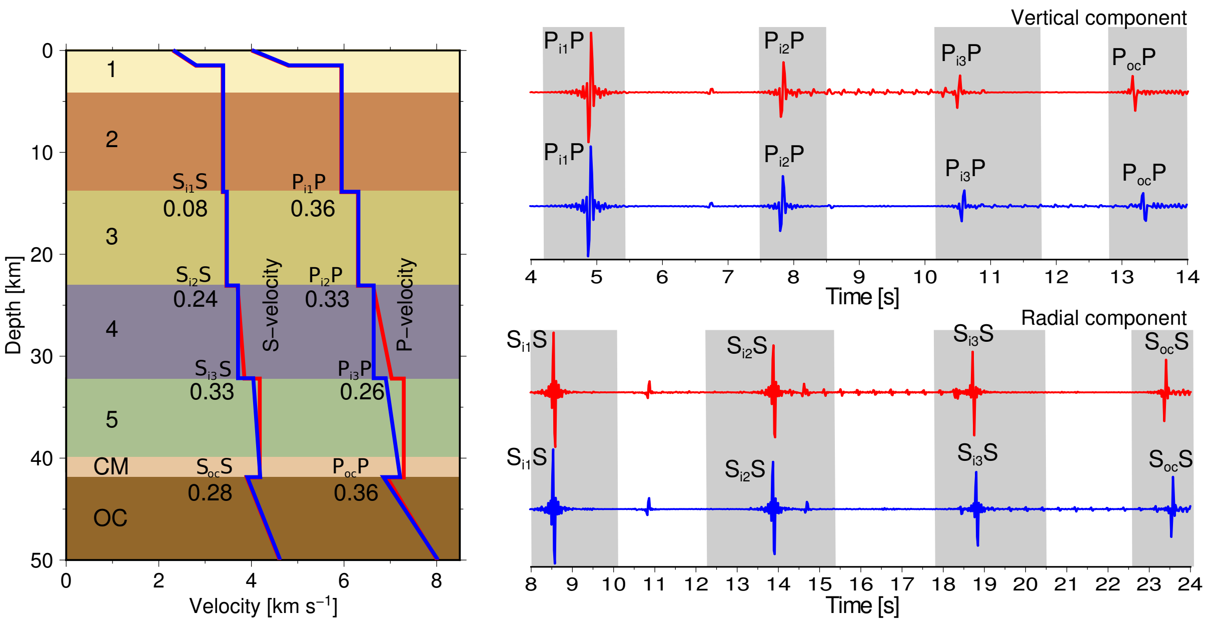

Figure 10: Left: synthetic 1D P- and S-velocity models found to reproduce the observed mean amplitude ratios in the eastern profile (EP). The numbers indicate the absolute values of the velocity contrasts at each interface in km s^{-1}. Note the low velocity zone (LVZ) at 42 km depth. The seismic velocity models were plotted in different colours to highlight the differences between them. The colours and numbers of the layers indicate the inferred lithological units (see Section 6.3 and Fig. 11). OC: oceanic crust; OM: oceanic mantle. Right: synthetic seismograms with the modelled reflectivity phases. Their colours correspond to those of the seismic velocity models used to produce them. The grey shading shows the time windows where the reflection phases were observed in the time-stacked images.

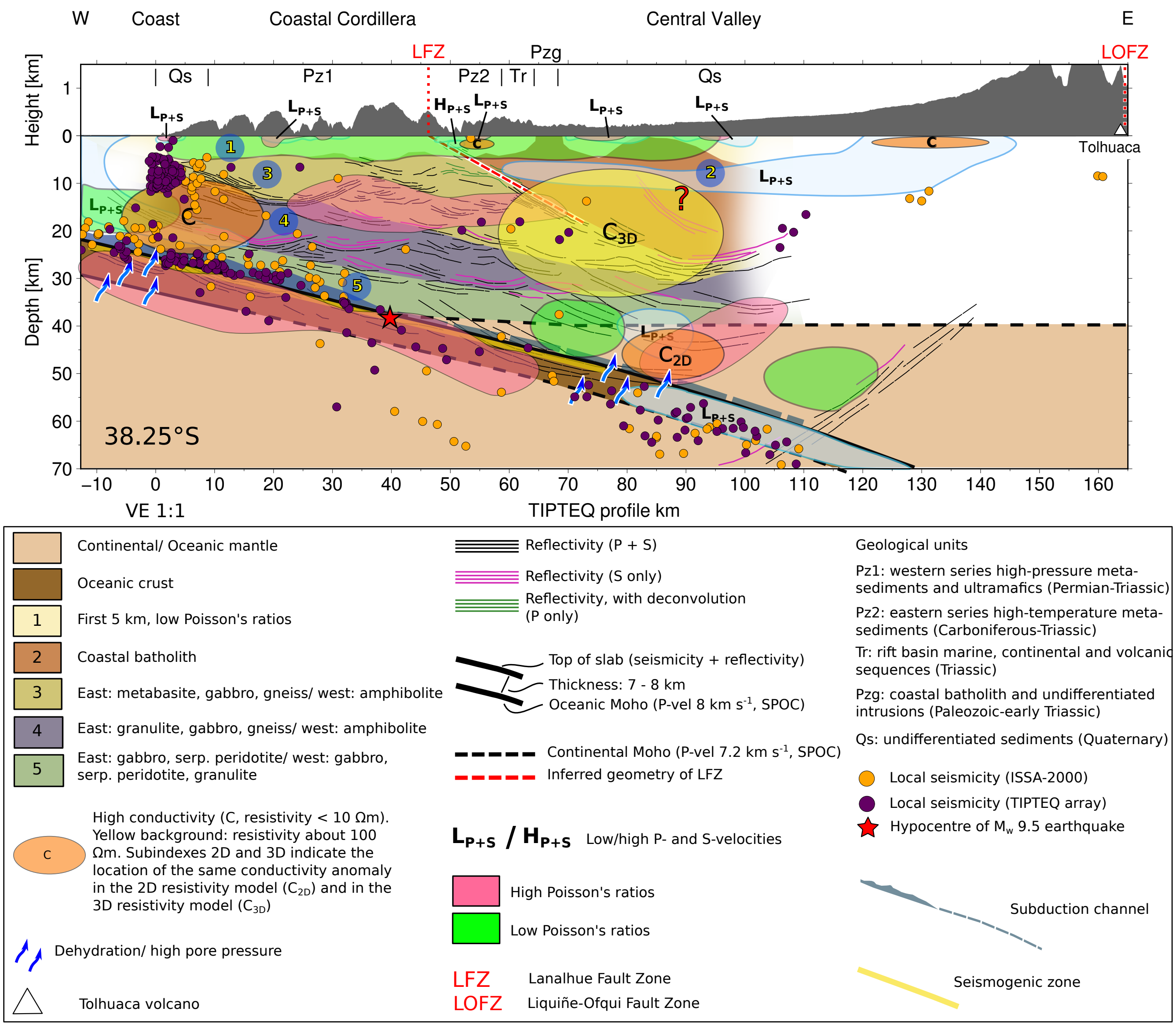

Figure 11: Integrative interpretation of the geometry, composition and processes in the southern Chile subduction zone along 38.25°S. Geological units taken from Melnick and Echtler (2006). LFZ: Lanalhue Fault Zone. LOFZ: Liquiñe-Ofqui Fault Zone.

Tables

Processing step	P-reflectivity processing	S-reflectivity processing
Data input	first 50 s of Z-component NVR data	first 50 s of EW- and NS-component NVR data to be processed separately
Common pre-processing	Data demeaned, useless traces killed, noise with frequencies in the range of useful frequencies muted (e.g. airblast, car noise), shift errors corrected, direct and refracted arrivals muted, static corrections moved traces to floating datum	
Polarity reversal	-	For traces with negative offset
Bandpass filter	6 - 10 - 35 - 50 Hz	4 - 8 - 20 - 40 Hz
Automatic gain control (AGC)	Window length: 4 s	Window length: 7 s
Coherence enhancement	Limited aperture Tau-P transform	Complex Wiener unit prediction filter for a specified frequency range, limited aperture Tau-P transform
Normal moveout (NMO) correction	Using SPOC velocity model (Krawczyk et al., 2006)	Using empirical S-wave velocity model (see text for details)
Common depth point (CDP) stack		
Post-stack processing	Static corrections take reflections to final datum, limited aperture Tau-P transform	Static corrections take reflections to final datum, time and space large variant bandpass filter
Kirchhoff depth migration		

Table 1: Workflow for the post-stack depth migration for P-reflectivity (vertical component, left) and S-reflectivity (horizontal components, right).

Supplementary figures

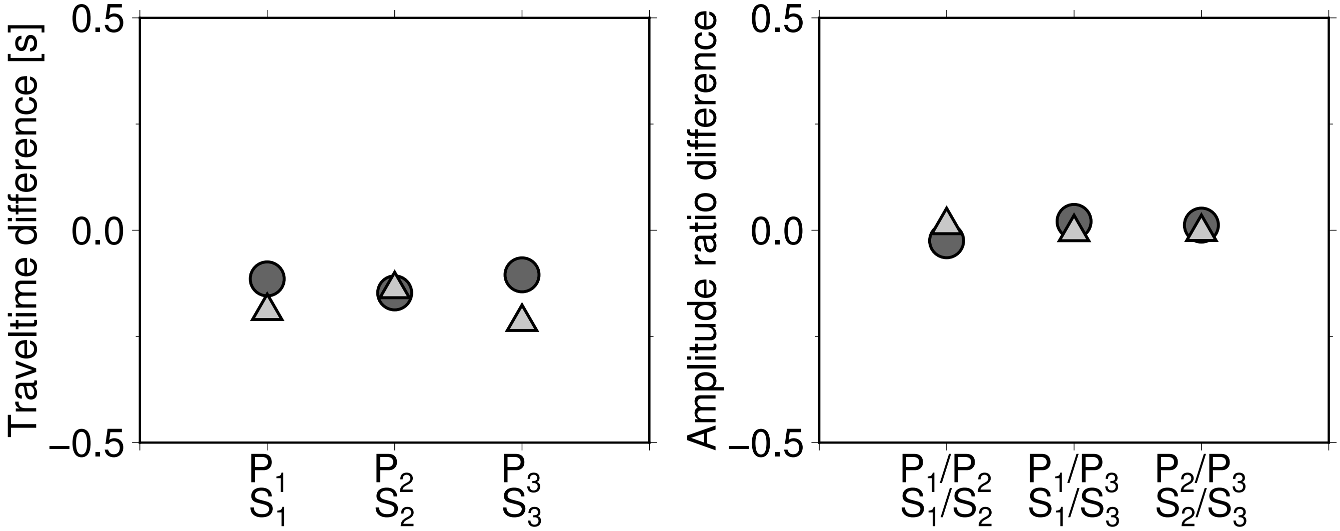

Figure S1: Differences in traveltimes (left) and amplitude ratios (right) for three reflections (and pairs of reflections) from a flat model and a dipping layer model. Circles: traveltime and amplitude ratio differences of P-reflections in the vertical component of the synthetic seismograms (flat model minus dipping layer model). Triangles: traveltime and amplitude ratio differences of S-reflections in the radial component of the synthetic seismograms (flat model minus dipping layer model).

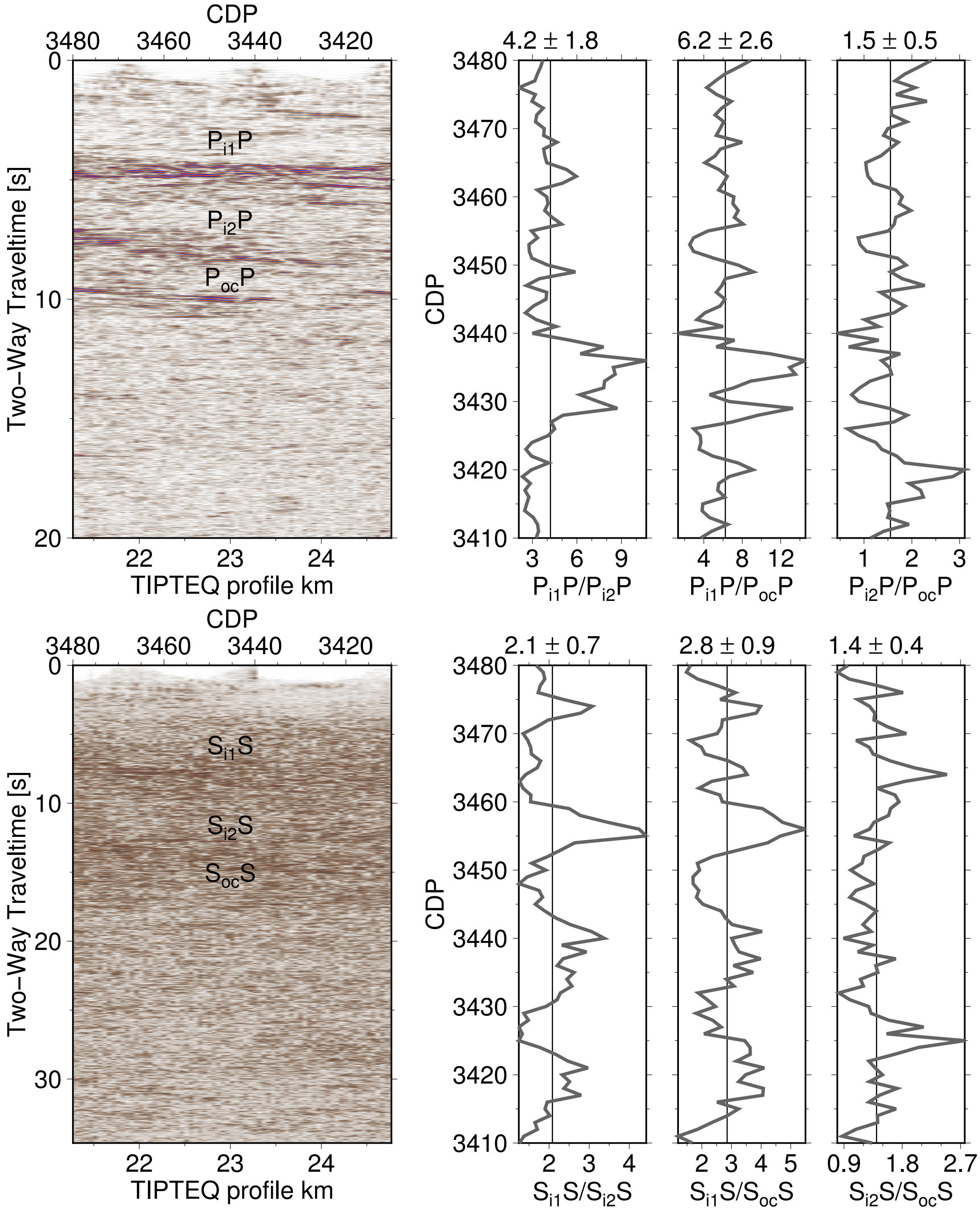

Figure S2: Upper panels: for the western 1D profile, WP, the three P-reflections, whose arrival times and amplitude ratios were modelled using the reflectivity method. The right panel shows the observed amplitude ratios for each CDP, with their mean observed amplitude ratio and standard deviation. Lower panels: equivalent observations for the three S-reflections.

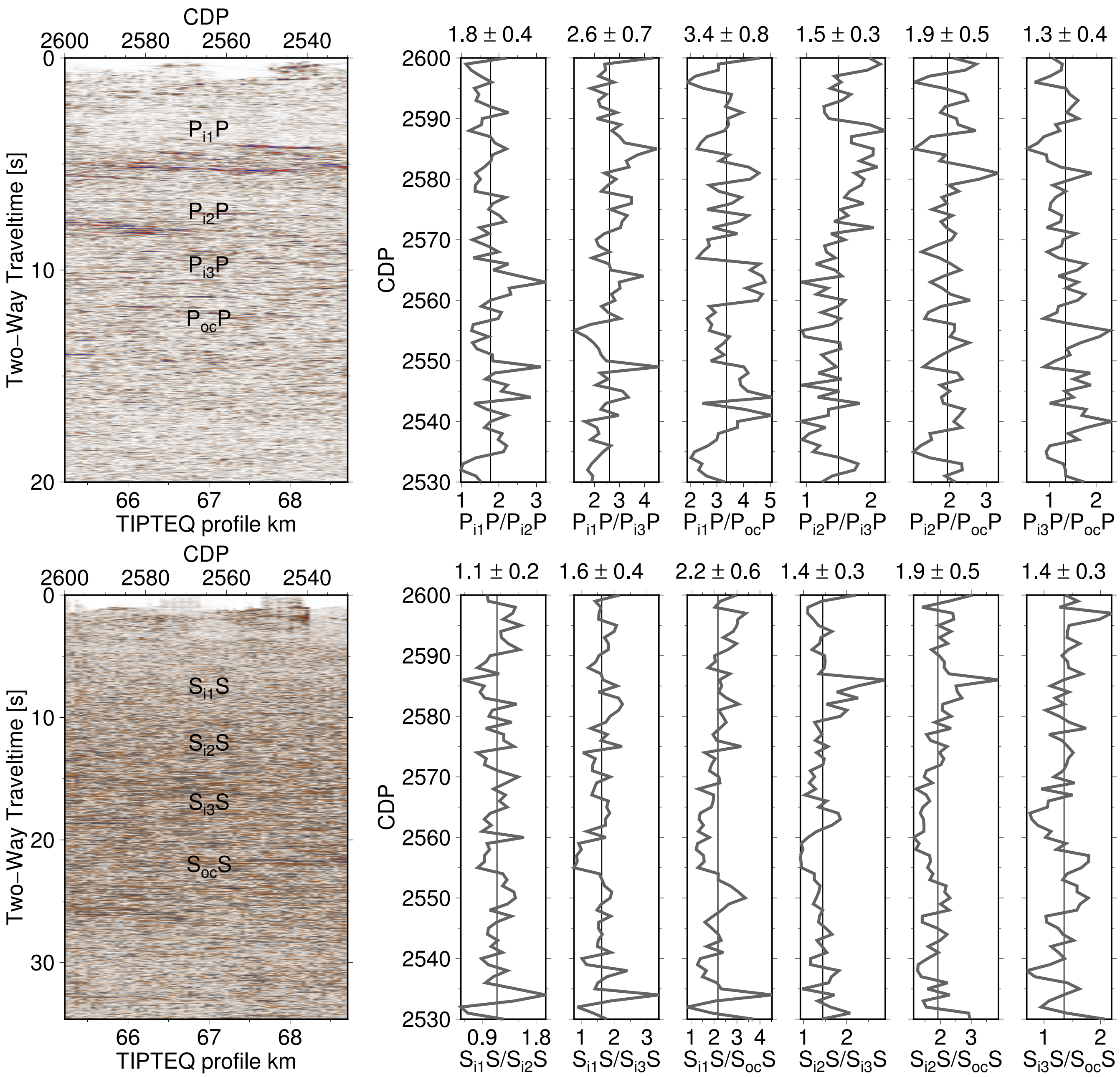

Figure S3: Upper panels: for the eastern 1D profile, EP, the four P-reflections, whose arrival times and amplitude ratios were modelled using the reflectivity method. The right panel shows the observed amplitude ratios for each CDP, with their mean observed amplitude ratio and standard deviation. Lower panels: equivalent observations for the four S-reflections.

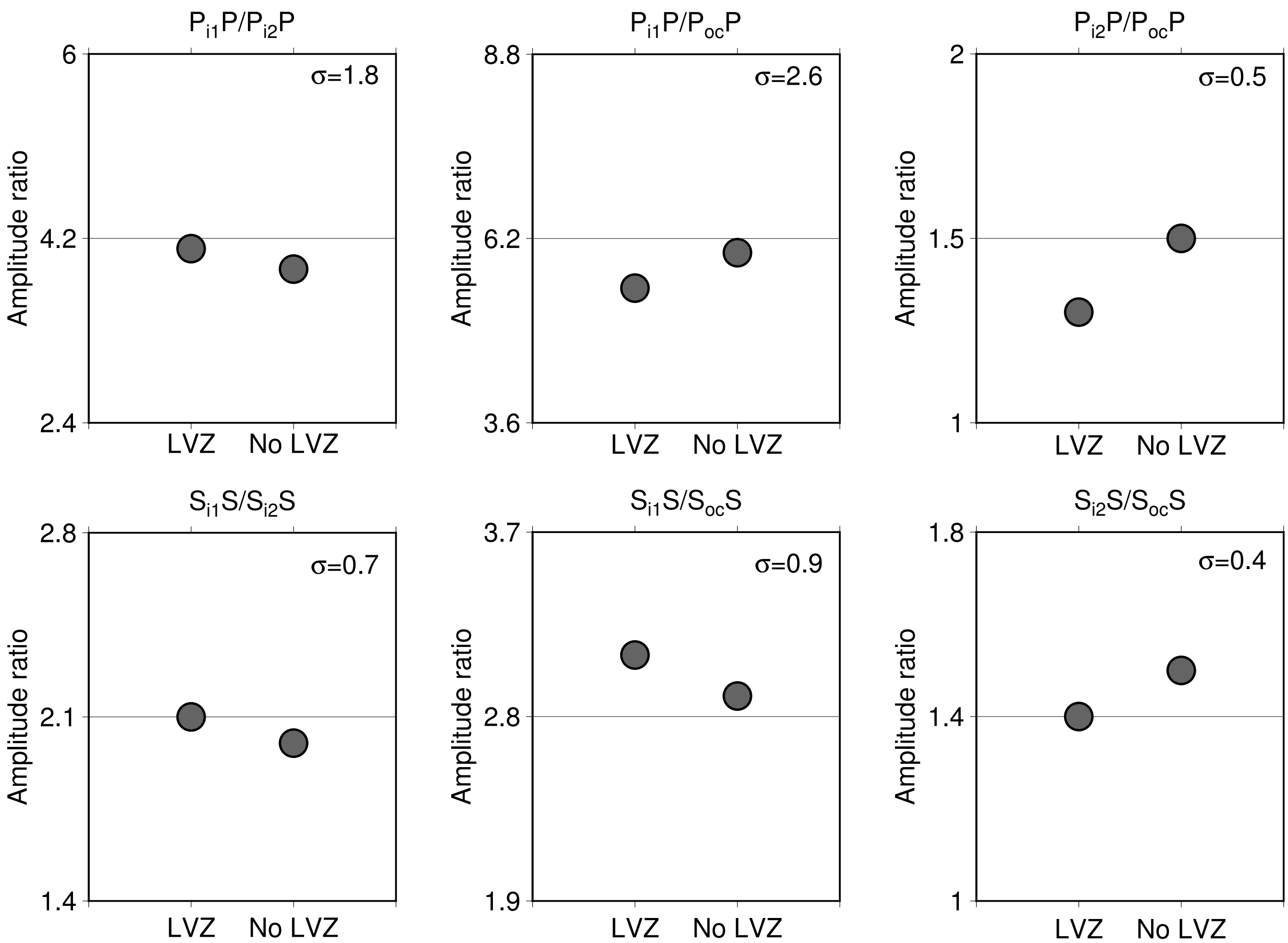

Figure S4: Top: calculated P-amplitude ratios for the 1D velocity models with a low velocity zone (LVZ) and without (no LVZ) for the western profile (WP). The line in the centre of each plot marks the observed mean amplitude ratio. The standard deviation (σ) is shown in each case. Bottom: calculated S-amplitude ratios.

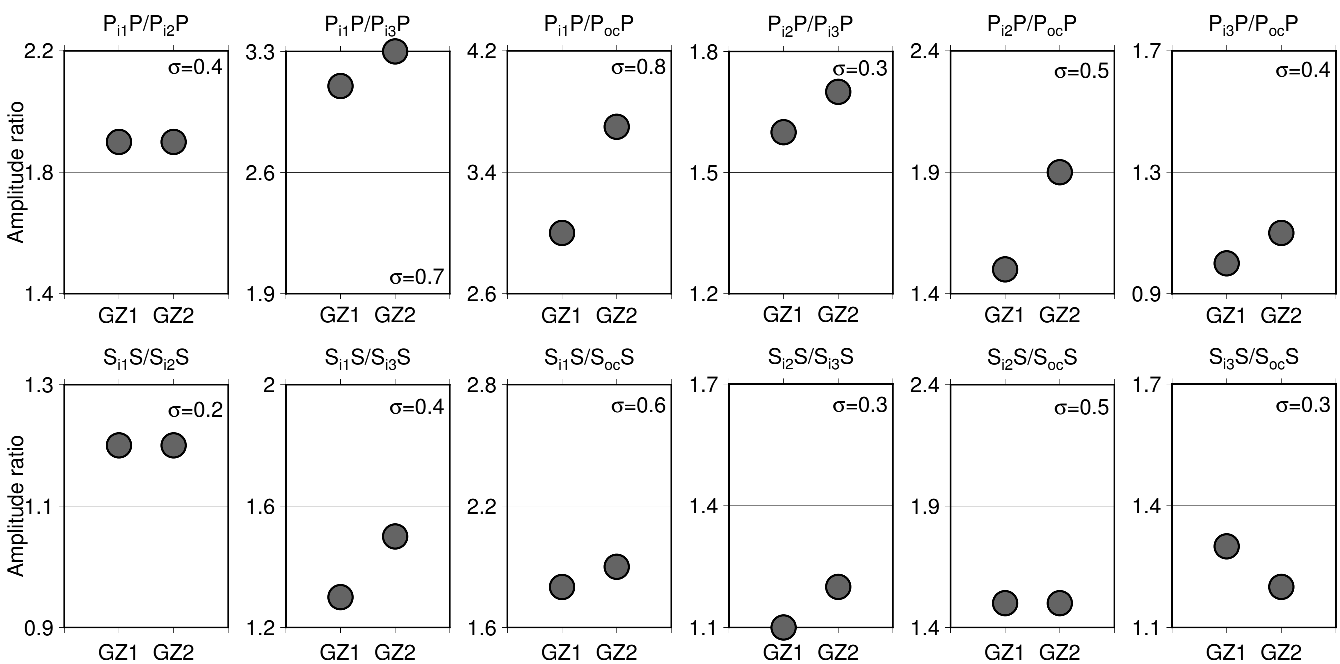

Figure S5: Top: calculated P-amplitude ratios for the 1D velocity models for the eastern profile (EP): the first with a gradient zone between the second and third intracrustal reflections (GZ1) and the second with a gradient zone between the third intracrustal reflection and the reflection from the top of the oceanic crust (GZ2). The line in the centre of each plot marks the observed mean amplitude ratio. The standard deviation (σ) is shown in each case. Bottom: calculated S-amplitude ratios.